J. Fluid Mech. (2015), *vol.* 777, *pp.* 122–150. © Cambridge University Press 2015
doi:10.1017/jfm.2015.318

Experiments on standing waves in a rectangular tank with a corrugated bed

Patrick D. Weidman[1,†], Andrzej Herczynski[2], Jie Yu[3] and Louis N. Howard[4]

[1]Department of Mechanical Engineering, University of Colorado, Boulder, CO 80309-0427, USA

[2]Department of Physics, Boston College, Chestnut Hill, MA 92467-3811, USA

[3]Civil Engineering Program, Department of Mechanical Engineering, School of Marine and Atmospheric Sciences, Stony Brook University, Stony Brook, NY 11790, USA

[4]Department of Mathematics, Massachusetts Institute of Technology, Cambridge, MA 02139, USA

(Received 1 July 2014; revised 28 May 2015; accepted 7 June 2015;
first published online 16 July 2015)

An experimental investigation of resonant standing water waves in a rectangular tank with a corrugated bottom is reported. The study was stimulated by the theory of Howard & Yu (*J. Fluid Mech.*, vol. 593, 2007, pp. 209–234) predicting the existence of normal modes that can be significantly affected by Bragg reflection/scattering. As a result, the amplitude of the standing waves (normal modes) varies exponentially along the entire length of the tank, or from the centre out in each direction, depending on the phase of the corrugations at the tank endwalls. Experiments were conducted in a 5 m tank fitted with a sinusoidal bottom with one adjustable endwall. Waves were excited by small-amplitude sinusoidal horizontal movement of the tank using an electrical motor drive system. Simultaneous time-series data of standing oscillations were recorded at well-separated positions along the tank to measure the growth in amplitude. Waveforms over a section of the tank were filmed through the transparent acrylic walls. Except for very shallow depths and near the tank endwalls, the experimental measurements of resonant frequencies, mean wavelengths, free-surface waveforms and amplitude growth are found in essential agreement with the Bragg resonant normal mode theory.

Key words: surface gravity waves, waves/free-surface flows

1. Introduction

Waves over variable topography have been studied by various techniques for a long time, particularly in the last thirty years. These studies are a natural extension of the classical theory of waves over a horizontal flat bottom, and are also important for applications to waves in oceans, lakes, rivers and estuaries. When the relevant length scales of the fluid motion are large compared to the water depth, fairly tractable models using shallow-water theories are appropriate, although on planetary scales rotational effects are usually an important complication. If the waves are short compared to the depth, bottom variations are essentially irrelevant. The intermediate

† Email address for correspondence: weidman@colorado.edu

case, where wavelength, depth and bottom variations have comparable scales, is more complex. Initial studies have revealed that propagating surface waves can be excited by corrugated seabeds, particularly when the number of submerged sandbars is large and when the free-surface wavelength is approximately double that of the bottom corrugations. This has come to be known as Bragg resonance of surface waves by periodic seabeds.

Theoretical studies of the Bragg phenomenon, as it applies to seabed–wave interaction, began with Davies (1980, 1982), who considered the reflection of surface water waves incident upon an undulating seabed, showing that, even with relatively few bottom corrugations, very substantial wave reflection can occur if the wavenumber of the bottom topography is approximately twice the free-surface wavenumber. He used regular perturbation theory based on the amplitude of the bottom corrugations and noted a singularity in this approach when the water wavelength was near twice the corrugation spacing, and was apparently the first to note '... analogies in solid state physics concerning the vibration of atomic lattices, a special case of which is Bragg reflection of X-rays from a crystal plane...'. Riley (1984) also noticed this singularity about the same time, but did not further investigate it, as he had other objectives in view. Davies & Heathershaw (1983, 1984) considered wave reflection from sinusoidally varying topography using linear perturbation theory and, for the first time, associated the name 'Bragg' with the fluid dynamic resonance between surface waves and bottom ripples. Mei (1985) used a multi-scale perturbation approach to clarify the situation near this 'resonance', which is now usually described as water wave Bragg resonance, reflection, or scattering. Kirby (1986*a*) investigated the problem by numerical integration of a model equation for waves propagating over a corrugated bottom, thus verifying and improving on the analytical results reported in Davies & Heathershaw (1984). In a follow-on paper, Kirby (1986*b*) investigated the gradual reflection of weakly nonlinear Stokes waves in regions of varying topography. A contribution towards understanding the experiments of Heathershaw (1982) discussed below, and one that complements and improves upon the theory of Davies & Heathershaw (1984), is the theoretical study of Benjamin, Boczar-Karakiewicz & Pritchard (1987) in which new experiments were also reported. Some time later, Kirby (1993) elucidated numerically the reflection of linear surface waves by sinusoidal bars in the case when the incident wave frequency is not necessarily close to resonance.

Using Mei's asymptotic method, Yu & Mei (2000*a*,*b*) extended the work of Bailard, DeVries & Kirby (1992) to investigate waves passing over a periodic array of sandbars and then (partially) reflecting from a beach or seawall. They demonstrated that the resulting partially standing waves over the periodic bed depended sensitively on the effective position of the shore reflection with respect to the phase of the bed corrugations, at least when the incident waves had a length near twice the sandbar spacing. In particular, though waves of length nearly twice the sandbar spacing would be largely reflected and so reduced in amplitude at the end of the sandbar patch, they could in fact be enhanced at a reflective beach if the proper phase relationship of the beach reflection and the bar patch were to occur. This was followed up in Howard & Yu (2007) (hereafter HY2007), who considered normal modes of a stationary rectangular tank with a corrugated bottom. When the corrugations are relatively small, most of these normal modes are only slight perturbations of the flat-bottom modes, in both their frequencies and their eigenfunctions. But a few of them, whose frequencies correspond to propagating waves of wavelength about twice the corrugation spacing, are strongly affected by the collaborative effects of

Bragg reflection, and their eigenfunctions can be considerably modified (though their frequencies are little perturbed). As shown in HY2007, these modifications depend sensitively on the position of the endwalls of the tank with respect to the phase of the bottom corrugations.

In order to set the stage for our experimental study, and the particular approach we employ, it is useful to briefly review experimental work on wave motion over corrugated-bottom topography. The first contribution, to our knowledge, was by Bagnold (1946), in a paper to which G. I. Taylor added a postscript note. Bagnold used a suspended plate connected to a rotating bar to excite standing waves over a sandy bottom in a water tank and observed the formation of bars, which he photographed. Sandbar growth and the interaction of surface water waves with an undulating seabed topography was studied, in considerable detail, by Heathershaw (1982) using resistance gauges. The results obtained were in remarkably good agreement with the linearized theoretical predictions of Davies (1980, 1982). The experiments performed by Davies & Heathershaw (1983, 1984) focused on the fluid flow over fixed artificial bars with flat beach at each end, and measured the reflection of incident waves. As noted above, these experimental studies were followed by Benjamin *et al.* (1987), who used rigid corrugations with a wave maker at one end of the tank and a plane sloping beach at the other. They obtained remarkably clean data for surface elevations in the range 0.1–0.2 mm using proximity transducers. Relying on another kind of gauge, the capacitance probe, Kirby & Anton (1990) measured reflection coefficients from a field of four artificial bars whose spacing could be varied with the flat segments between them and near the two ends. Soon afterwards, again utilizing resistance wires, O'Hare & Davies (1993) undertook a comprehensive study of both the evolution of sandbars and the interaction between them and the fluid flow over an erodible bed, with a sand patch positioned in the central section of the tank. Their experiments employed two kinds of sand, coarse and fine, and their data compared favourably with models and numerical simulations.

There are two broad goals of the present study which stand in sharp contrast to previous experimental work.

The first objective is to systematically explore the roles of the relative water depth and boundary conditions on waves passing over a fixed sinusoidal bed terminating abruptly at the endwalls. Thus the focus here is not on investigating sandbar formation or on simulating waves approaching shallow beaches as in the experiments reviewed above, but on the essential aspects of the Bragg phenomenon in its most fundamental form. The problem, as formulated mathematically in HY2007, does not include nonlinear effects. In this regard, it is also of interest to see how the physics of Bragg resonance changes as the surface of the water approaches the top of the corrugations. Although many critical aspects of standing waves near the Bragg resonance, including the direction(s) in which the amplitude increases, depend sensitively on the endwall boundary conditions, no previous experimental study has attempted to document this behaviour. Earlier experiments aimed more narrowly at modelling waves near shallow beaches and thus focused on progressive waves with small reflection at the ends.

The second objective is to test the existing mathematical analysis, map its limitations and stimulate new theoretical directions. The extant theory in HY2007, though linear, is far from transparent as it is formulated, and the results are obtained in a conformally transformed plane. As a result, the theoretical corrugation profile is not exactly sinusoidal; see figure 1. Furthermore, as pointed out in Yu & Howard (2012), there is strong evidence that the exact Floquet modes used in the theory form a complete basis and can be used to solve boundary-value problems in a manner

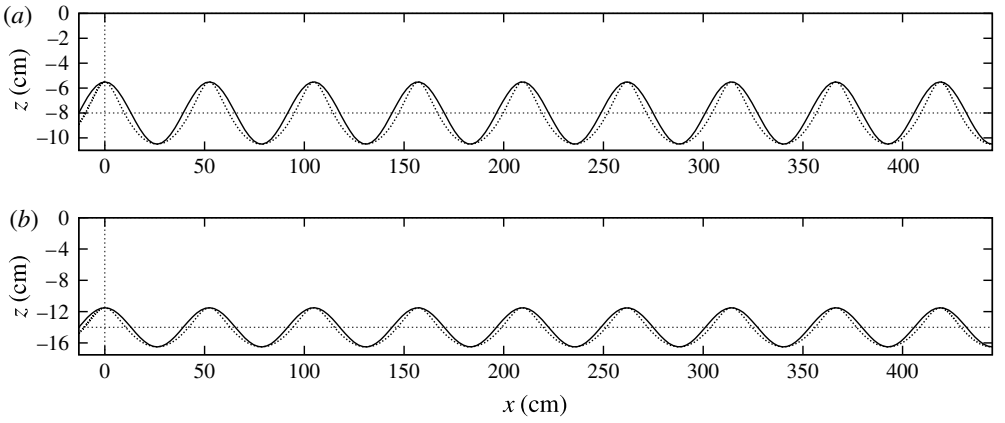

FIGURE 1. Comparison of the sinusoidal bottom used in the experiments (solid lines) with the theoretical corrugation profile (dashed lines) given by (2.1) for (*a*) $h = 8$ cm and (*b*) $h = 14$ cm. In each case, $z = 0$ is the undisturbed free surface and the different vertical scales should be noted. The right endwall position is that for configuration 1.

similar to the well-known set of propagating and evanescent waves over a flat bottom, but a formal mathematical proof is not yet available – thus our experiments provide a valuable test on this aspect. The experiments are also used to determine under what conditions the linear description may prove insufficient, showing how the actual flows differ from those predicted, thus paving the way for a nonlinear analysis and further experiments.

The experiments were designed specifically to test the dependence of resonant free-surface waveforms on the end phases of a sinusoidal bedform placed between the vertical endwalls of a rectangular tank. The length of the tank in our set-up could be changed by a quarter of a corrugation wavelength, so that, according to the theory, the longer tank would result in a surface wave amplitude varying exponentially from one end to the other (asymmetric configuration 1), whereas the slightly shorter tank would excite waves with amplitude varying exponentially from the centre out towards opposite endwalls (symmetric configuration 2). In each configuration, and for various water depths, the normal modes with frequencies near the first-order Bragg reflection condition were excited and the amplitudes of the standing waves were measured at two locations along the tank. Unlike earlier experimental investigations, we utilize new pressure probes to measure surface elevation, developed for this study. Additional data were collected using capacitance probes in order to validate the pressure probe data and provide an indication of experimental accuracy. Standing waves excited in the set-up were also filmed over a 1 m segment of the tank at various water depths, in both configurations, and detailed surface wave profiles were numerically extracted; this experimental method has not previously been applied in Bragg resonance studies.

The organization of the paper is as follows. In § 2 we review briefly the theory in HY2007 to provide predictions of the normal modes for the two configurations of our experiment. In § 3 we describe in detail the experimental set-up, including the apparatus, the mechanical drive system and the data acquisition systems. Results presented in § 4 include sample time series of standing waves and free-surface waveforms. Measured frequencies, amplitude ratios and mean wavelengths are given for the relevant normal modes of the tank, i.e. those whose natural frequencies are

sufficiently close to the Bragg frequency so that the cooperative effects of bottom corrugations are significant. Additionally, frequency response curves are given to suggest the precision to which the Bragg resonant normal mode frequencies can be experimentally defined. All results are compared with theoretical predictions. We conclude with a summary and discussion in § 5. Appendix A provides the theory of operation of the new pressure wave gauges and an error analysis for their application to the measurement of the amplitude ratios in this experiment.

2. Review of theoretical results

2.1. *Background*

Until recently, the only known complete basis of linear modes for water waves was for the case of two-dimensional time-periodic motions for constant depth over a flat horizontal bed. This complete set of modes is usually described as two oppositely directed propagating waves and two infinite families of evanescent waves. It has played important roles in various boundary-value problems, in particular in engineering applications.

For periodic bottom topographies, the studies given in HY2007 and Yu & Howard (2010, 2012) have provided a new approach. Two principal ideas are involved: (*a*) use of a conformal map of the flow domain to a strip, and (*b*) use of the general ideas of the Floquet theory to exploit the spatial periodicity. HY2007 avoided some complexities of (*a*) by restricting attention to a particular family of bed profiles for which the conformal map was well known. By examining their behaviours as the bed becomes flat, connections are established between these exact Floquet solutions and the set of flat-bottom modes. A full treatment of the theory for arbitrary periodic bed profiles is given in Yu & Howard (2012), including the method of constructing the needed map. The familiar basis of flat-bottom propagating and evanescent waves is thus extended to the case of arbitrary periodic topographies. An application of this work to wave scattering with different boundary conditions is reported in Yu & Zheng (2012).

2.2. *The exact Floquet solutions*

Theoretical results from HY2007 are summarized here for comparison with experiments. The family of theoretical corrugations is given parametrically by

$$h_b(x) = \epsilon h \cos 2\xi, \quad \text{where } k_B x = \xi - \epsilon k_B h \coth(2k_B h) \sin 2\xi, \tag{2.1}$$

and $k_B \equiv \pi/\lambda_{bar}$ with λ_{bar} being the corrugation wavelength. The amplitude parameter ϵ satisfies the inequality $\epsilon < \tanh(2k_B h)/(2k_B h)$, so that $h_b(x)$ is single-valued. The conformal transformation between the (x, z) plane and the mapped plane (ξ, η) is given by

$$k_B x = \xi - \epsilon b \sin 2\xi \cosh 2\eta, \quad k_B z = \eta - \epsilon b \cos 2\xi \sinh 2\eta, \tag{2.2a,b}$$

where $b = k_B h/\sinh(2k_B h)$. Under the transformation, the undisturbed flow domain $-h + h_b(x) \leqslant z \leqslant 0$ is mapped into $-k_B h \leqslant \eta \leqslant 0$. The periodicity of the problem is retained. The theoretical bed profile in (2.1) is shown in figure 1 for $h = 8$ and 14 cm, and compared with the sinusoidal bottom used in the experiments. The theoretical profiles are approximately sinusoidal but exhibit smaller curvature at the troughs and

larger curvature at the crests. The ratios $|\Delta z/a_{bar}|$ at the midpoint between trough and crest are 0.37 and 0.30 for $h = 8$ and 14 cm, respectively.

For linear time-periodic motion, the velocity potential is $\phi = \varphi(x, z)\mathrm{e}^{-\mathrm{i}\omega t} + \text{c.c.}$, where ω is the angular frequency. In the mapped plane, the Laplace equation for φ is solved satisfying the transformed boundary conditions at the free surface $\eta = 0$ and at the bed $\eta = -k_B h$. The solution is given as follows:

$$\varphi(\xi, \eta; \mu) = \mathrm{e}^{\mu\xi} \sum_{n=-\infty}^{\infty} D_n \mathrm{e}^{\mathrm{i}n\xi} \frac{\cosh\left[(n - \mathrm{i}\mu)\,(\eta + k_B h)\right]}{\cosh\left[(n - \mathrm{i}\mu)\,k_B h\right]}, \tag{2.3}$$

$$L_n D_n = D_{n-2} + D_{n+2}, \tag{2.4}$$

$$L_n = (\epsilon b)^{-1}\left\{1 - g k_B \omega^{-2}\,(n - \mathrm{i}\mu)\tanh\left[(n - \mathrm{i}\mu)\,k_B h\right]\right\}. \tag{2.5}$$

Equation (2.3) represents a set of solutions, individually identifiable by the Floquet exponent μ. It is not a separable solution in the mapped domain, as the individual terms of the sum do not satisfy the free-surface condition. For a given frequency ω, the requirement that (2.4) be satisfied by a sequence of non-trivial $D_n(\mu)$ determines the values of μ (occurring in $\pm$ pairs). This is the dispersion relationship for linear Floquet modes, equivalent to that in the flat-bottom case.

The analogues of flat-bottom evanescent waves are themselves reasonably called 'evanescent', for they always decay rapidly in $\pm x$ directions (due to the large values of real $\pm\mu$), and so play significant roles only near the lateral boundaries. However, the analogues of flat-bottom propagating waves are a little different. The two-parameter family ($\pm\mu$) of 'propagating waves' is, as a whole, analogous to linear combinations of left- and right-propagating waves because there is always some scattering by the corrugations. In the (ω, ϵ) plane, the frequencies for the propagating wave modes are separated by isolated bands near the Bragg frequency $\omega_B^2 = g k_B \tanh k_B h$ or similar higher-order Bragg frequencies, which we call 'resonance tongues'. When the frequencies fall within one of these bands, the propagating waves have real μ values (smaller than 1 in magnitude), hence their amplitudes modulate exponentially, but slowly, in space.

If we denote by $\varphi^{\pm}$ and $\varphi_j^{\pm}$ the Floquet solutions in (2.3) corresponding to the wave modes with $\pm\mu$ and evanescent modes with real $\pm\mu_j$ for a frequency ω, the normal mode in the tank for that frequency is given by

$$\varphi = C^{+}\varphi^{+} + C^{-}\varphi^{-} + \sum_{j=1,\infty} (C_j^{+}\varphi_j^{+} + C^{-}\varphi_j^{-}), \tag{2.6}$$

where the coefficients $C^{\pm}$ and $C_j^{\pm}$ are determined by satisfying the boundary conditions at the tank endwalls, $x = x_0$ and $x = x_0 + L$. Let $\alpha = k_B x_0$, $\beta = k_B L - N\pi + \alpha$ and N be the nearest integer number of corrugation wavelengths to the actual length of the tank (HY2007). Thus, relative to the corrugation crests, α is the phase at the left endwall and β is the phase at the right endwall. Under the conformal transformation, the two endwalls are mapped into the curves $\xi = \xi_0(\eta)$ and $\xi = N\pi + \xi_1(\eta)$, respectively, where

$$\alpha = \xi_0 - \epsilon b \sin 2\xi_0 \cosh 2\eta, \quad \beta = \xi_1 - \epsilon b \sin 2\xi_1 \cosh 2\eta, \tag{2.7a,b}$$

according to (2.2*a*). Since the mapping is conformal, it remains that $\partial\varphi/\partial n = 0$ at $\xi = \xi_0(\eta)$ and $\xi = N\pi + \xi_1(\eta)$. The frequency ω, for which non-trivial C can be found

to satisfy these boundary conditions, is the natural frequency of the normal mode for the tank. In our experiments, we focus on ω inside the resonance tongue, close to ω_B. The free-surface elevation (i.e. eigenfunction) is obtained as

$$\zeta = -g^{-1}\partial\phi/\partial t \quad \text{at } z = 0. \tag{2.8}$$

We note that the normal mode eigenfunctions given in (2.6) are quite different from the corresponding modes of the flat-bottom tank. The natural frequencies are not significantly changed by the relatively small 'perturbation' of the corrugations. However, with a sufficient number of corrugations in the tank, the eigenfunctions of those modes with natural frequencies close to the Bragg resonance frequency may be considerably altered due to the cooperative effects of successive corrugations. Those modes will be of relatively high frequency, compared to the fundamental frequency of the tank. The eigenfunctions locally look like standing waves, but with oscillation amplitude varying exponentially along the length of the tank. The precise form of these exponential variations depends sensitively on the end phases of the corrugation, that is, on parameters α and β.

3. Experimental set-up

The experimental set-up is composed of the physical apparatus and the data acquisition system described in §§ 3.1 and 3.2 below. In these it is natural to use the English system of dimensions to describe components used to assemble the apparatus, but the metric system will be employed for all experimental data. The experimental procedure is outlined in § 3.2.

3.1. *Physical apparatus*

Figure 2 shows details of the apparatus, with the left half displayed above and the right half shown below. The clear polycast tank ① was fabricated in two 8′ sections. The rather long 16′ length was chosen to incorporate a sufficient number of bottom corrugations so that the amplitude growth along the channel could be detected. Before assembling the tank, a black indelible grid ② with 1 cm vertical and 2 cm horizontal spacings was scribed on the inner left wall for filming purposes. The two halves of the channel were sealed with rubber and cork gaskets and bolted together using 1/2″ plastic bolts, washers and nuts ③. The tank was mounted on top of the flat side of a 6″ × 3″ aluminium C-channel ④ with stops ⑤ mounted at opposite ends of the tank and numerous aluminium/balsa guides ⑥ to ensure perfect alignment.

The aluminium C-channel was suspended using three pairs of 1/16″ steel wire ropes ⑦ with compression eyelet sleeves. Assemblies ⑧ were designed to house two SR3-ZZEEC Boca bearings separated to accommodate the eyelets using a shoulder bolt as shown in detail ⑨. With the lower assemblies mounted on the C-channel, the upper assemblies were bolted to carefully levelled steel plates mounted on rafters in the garage of one of the authors (P.D.W.), where the experiments took place.

Substantial resistance to bending was attained by fixing a wooden 2″ × 4″ beam ⑩ along the bottom centre of the C-channel. Care in locating the suspension points is particularly important since the total weight of the C-channel and polycast tank filled with water to the highest 14″ depth used in the experiments was about 650 lb. A study was performed to ascertain the optimum points for mounting the suspension wires to provide least deflection under a uniformly distributed load. The 84″ length of the suspension wires was chosen so that the bottom of the wooden beam under the

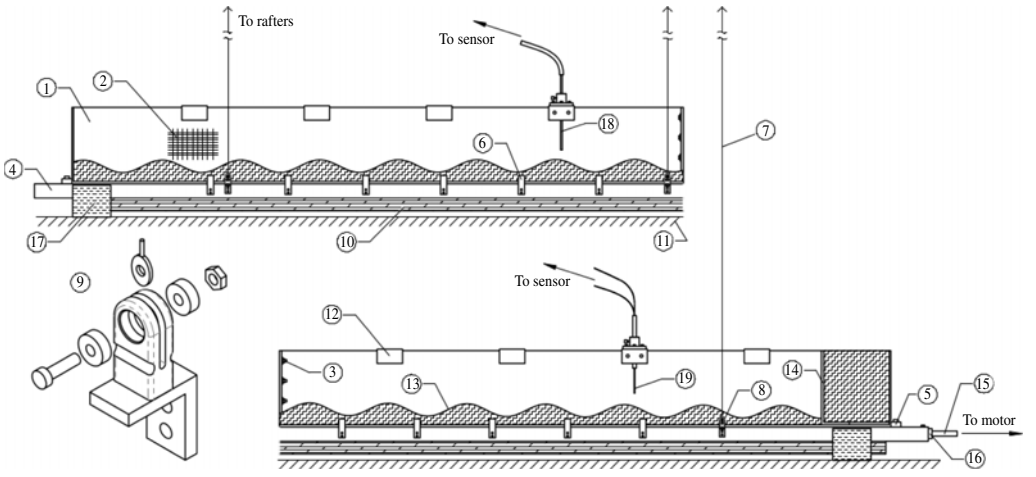

FIGURE 2. Sketch of the experimental apparatus. The circled numbers are items referred to and discussed in the text.

aluminium channel hovered above the garage floor (11) by about one inch. Owing to the flexibility of the $1/4''$ vertical sidewalls, the channel would bow outwards at high water level. This was ameliorated by placing rectangular brackets (12) at intervals on top of the channel.

The bed waveform (13) was fabricated using no. 2 density expanded polystyrene foam supplied to us in $6'$ lengths cut exactly $5''$ wide to fit snugly between the tank sidewalls. For the chosen wavelength $\lambda_{bar} = 52.36$ cm and amplitude $a_{bar} = 2.5$ cm, a pair of hardwood guides one wavelength long was machined to the shape

$$z(x) = 2.54 + a_{bar}[1 - \cos(2\pi x/\lambda_{bar})], \tag{3.1}$$

where x, z, a_{bar} and λ_{bar} are in centimetres. The 2.54 cm bottom thickness ensured rigidity of the cut foam pieces while handling. The foam sections were butted together and adhered to the bottom of the tank using industrial-strength double-sided adhesive tape to give the configuration 1 corrugation shown in figure 2. Configuration 2 was achieved by placing an inverted quarter-wavelength section of foam corrugation on top of the terminal quarter wavelength of the configuration 1 corrugation. In each case a false right endwall (14) was held in place using plastic clamps.

The waveform starting at the left at phase α and ending at the right at phase β has total length

$$L = [N + (\beta - \alpha)/\pi]\lambda_{bar}, \tag{3.2}$$

where N is the number of maxima. Fixing the left endwall phase at $\alpha = -\pi/4$, we can select the right endwall phase β and determine the appropriate N that corresponds to the total working length of the tank. For the asymmetric configuration 1 (cf. figure 2), $\beta = -\pi/2$ and $N = 9$, giving a working length $L = 8.75\lambda_{bar}$, i.e. $L = 458.2$ cm. Moving the right endwall inwards by $(1/4)\lambda_{bar}$, we obtain the symmetric configuration 2 for which $L = 8.5\lambda_{bar}$, i.e. $L = 445.1$ cm, corresponding to $\beta = -\alpha$ and $N = 8$. These configurations were chosen to have the highest spatial growth rates of the resonant surface waves.

The second component of the apparatus is the periodic drive system. We adapted the reciprocating drive system used by Davis & Weidman (2000). The motor mounted

on a heavy horizontal platform was geared 3:1 to a reciprocating rod (15) of length $l = 65$ cm, which could be continuously offset from its drive shaft to deliver very nearly sinusoidal motion with peak-to-peak strokes as large as $1/4''$. For these small strokes, Davis & Weidman (2000) have shown that the power in the first harmonic is 10^{-6} times the power delivered at the fundamental frequency. The opposite end of the reciprocating rod was fixed via a wrist pin (16) housed on the right bottom end of the aluminium channel.

The maximum frequency for horizontal oscillation was 150 r.p.m. For the water depths reported here, the highest theoretical first-mode Bragg frequency in both configurations is about 50 r.p.m. and second-mode frequencies achieve nearly 100 r.p.m. The drive system was equipped with a revolution (r.p.m.) indicator whose LED readout refreshed every one or two seconds for the measurements reported here. Alignment of the natural path of tank motion was maintained using wooden guides (17) secured to the garage floor at opposite ends of the C-channel ④.

3.2. *Data acquisition procedure and timeline*

Water depths $h = 8,\ 9,\ 10,\ 11,\ 12,\ 13$ and 14 cm were selected for experimentation. The amplitude of the waves excited at Bragg resonance depends on the stroke imparted by the reciprocating rod. Since the procedure for changing the stroke for each new water depth is very time-consuming, we performed a set of experiments to determine the 'best average stroke' for the seven water depths. Large strokes yielded nonlinear waves at high depths and small strokes made it difficult to visually ascertain the nodes of free-surface oscillation necessary for wavelength measurement and for positioning the wave gauges. For all measurements presented here the chosen stroke was $2X_0 = 0.116''$, giving sinusoidal tank motions $X_0 \sin \omega t$.

Two measurement systems were employed to record the amplitude ratio of two well-separated wave crests. In the first system, simultaneous time-series pressure measurements were recorded from two spatially separated PASCO low-pressure sensors (model CI-6534A) connected via tygon tubing to $3/32''$ inner diameter brass tubes (18) submerged 2 cm below the quiescent free surface. Since the probes were removed during each adjustment to a new water depth, care was taken to remove water droplets trapped in the brass tubes before re-immersion; generally the brass tubes were blown dry with air from a pressurized canister. The probes, always placed at experimentally observed locations of wave crests, were widely separated to obtain large differences in wave amplitude. For configuration 1 where the amplitude grows monotonically, the probes were placed at the second crest in from each endwall, giving a separation distance $2.5\overline{\lambda}_e$, where $\overline{\lambda}_e$ is the experimentally measured average free-surface wavelength. For configuration 2, where the wave amplitude grows from the centre of the tank towards each endwall, one probe was placed at the first crest to the left of centre and the other was located $2\overline{\lambda}_e$ to its right. A theoretical analysis of the pressure calibration and rise height of liquid inside the brass tube is given in appendix A. The results give 0.08896 kPa cm^{-1} for probe 1 and 0.08888 kPa cm^{-1} for probe 2.

The second measurement system incorporates high-frequency, capacitance-type wave gauges (19) borrowed from Penn State University. The water-penetrating portion of the gauge consists of a 1.6 mm outer diameter glass tube, which contains a conductor and is sealed at the underwater end. Details on the electronic conditioning of the signal may be found in Henderson & Hammack (1987). A direct calibration for the capacitance probe gave 2.268 V cm^{-1} with a goodness of fit $R^2 = 0.99832$.

Another objective is to obtain free-surface waveforms over an oscillation period. This was accomplished using a Canon Vixia HF G10 high-definition camcorder to capture the free-surface waveform over a segment approximately 1.5 m in length ($\sim 3\lambda_{bar}$) near the left end of the tank where the grid ② is scribed. To enable automated extraction of the interface shapes from the video stills, the water was dyed deep red to create strong contrast with the white background above the water surface obtained by backlighting a frosted plastic plate using a $12'' \times 60''$ Fawoo LED light panel. A series of still frames corresponding to two or three oscillation periods was saved from the video. Each frame was analysed using a MATLAB program, which returned the x–y coordinates of the interface. The horizontal resolution of this procedure was one pixel and the interface between water (red) and air (white) was discerned by sampling pixel intensities along vertical columns one pixel wide, with a carefully defined threshold intensity value. The interface data were then numerically smoothed to remove discontinuities due to finite pixel size and inaccuracies of assigning individual pixels to either water or air using the threshold.

After construction of the apparatus, initial experimentation with wire conductance probes borrowed from Woods Hole was carried out. We observed some measurement sensitivity to the change in contact angle of the meniscus as the wave changed direction. Thus, to improve measurement accuracy, we switched to the sensitive PASCO pressure sensors in 2010. After an initial series of measurements taken in June/July 2011, careful measurements were taken during August/September 2011 (Data Set 1) and in January 2012 (Data Set 2). Owing to an outlier in the amplitude ratio measured using the pressure probes, a final set of measurements was made using capacitance probes in July 2013 (Data Set 3).

The experimental procedure for Data Set 1 was as follows. After adding water, measurements of a liquid level (± 0.3 mm) were made from bedform crests at opposite ends of the tank using a millimetre steel ruler and adjustments were made to attain the desired liquid depth. With the pressure probes immersed 2 cm below the quiescent free surface, the tank was set into motion to determine the mode 1 resonance frequency visually so the probes could be set at appropriate waveform crests. A period of some minutes was required for the temperature of the brass tubes to equilibrate with the water temperature. The effect of the temperature inequality was reflected in a gradual change in pressure monitored on a laptop.

As the motor warmed, its frequency increased ever so slowly. With the motor drive frequency set just below the nominal Bragg resonance frequency, the pressure signal rose to its maximum, at which point 20–30 s time series for each probe were recorded simultaneously. The same procedure was followed for all other water depths and for Data Sets 2 and 3 in both configurations.

For Data Set 3, however, a malfunction in one of the ship-to-shore electronics systems left us with just one probe. Therefore, at each fluid depth, a resonance amplitude time series was recorded at a prescribed crest, the motor was stopped, and the probe was moved to the other crest position. The motor was restarted and the second resonance time series was recorded, endeavouring to set the frequency as close as possible to the resonance frequency. Then frequencies for the two data sets were, on average, within 0.03 %, with some differences being as large as 0.05 %.

4. Presentation of results

4.1. *Frequencies*

As a preliminary test on the behaviour of the system (using the original motor), we measured several odd-mode frequencies for our flat-bottom tank of length

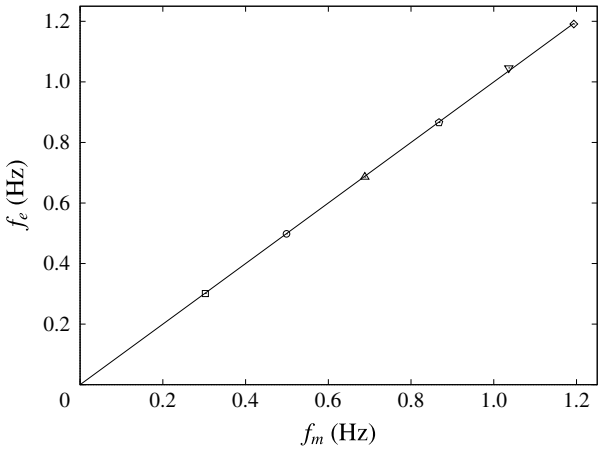

FIGURE 3. Measured odd normal mode frequencies f_e in the flat-bottom tank with $L = 487.7$ cm at water depth $h = 10$ cm plotted against the theoretical frequencies f_m for $m = 3$ (square), 5 (circle), 7 (up triangle), 9 (pentagon), 11 (down triangle) and 13 (diamond). The theoretical frequencies f_m are computed using (4.1) and the diagonal line for exact agreement is shown for comparison.

$L = 487.7$ cm at water depth $h = 10$ cm. Standard potential theory (Milne-Thomson 1962) gives the theoretical frequencies f_m (in Hertz)

$$f_m = \sqrt{g\, k_m \tanh(k_m h)}/2\pi, \tag{4.1}$$

where $g = 980$ cm s^{-2} and $k_m = m\pi/L$ for $m = 1, 3, 5, \ldots$. Measurements were obtained by gently sweeping though the expected resonance frequency with the drive motor system and noting the frequency at which the largest amplitude of standing wave motion was observed. The results presented here represent an average of three such measurements for each mode m. Experimentally we find that the windows for these resonance frequencies are quite sharp, so the measured frequencies can be obtained to considerable accuracy.

The experimentally measured values f_e for modes 3, 5, 7, 9, 11 and 13 of the flat-bottom tank are plotted against the theoretical values f_m in figure 3; in this presentation the diagonal gives exact correspondence between measurement and theory. The lowest-frequency mode $f_1 = 0.1015$ Hz was not accessible using the original motor, which had a top speed four times faster than the gear reduction motor used for all other experiments reported here. Analysis of the data shows that the mean value of the absolute difference between measured and theoretical frequencies is 0.37 %.

We now turn to the Bragg resonant normal mode frequencies. The standing wave frequencies were measured at each water depth in both configurations. Figure 4 displays the variation with depth of the experimentally measured frequencies f_e from Data Set 1 compared with the theoretical predictions f_t. The frequencies of the corresponding flat-bottom mode f_9 are also shown. For both configurations $f_9 > f_t > f_e$. Analysis of these data shows that, on average, the experimental frequencies are 1.29 % below theory for configuration 1 and 1.60 % below theory for configuration 2. The theoretical frequencies f_t of the corrugated-bottom tank remain fairly close to the flat-bottom frequencies f_9, both of which vary linearly with depth. For configuration 1

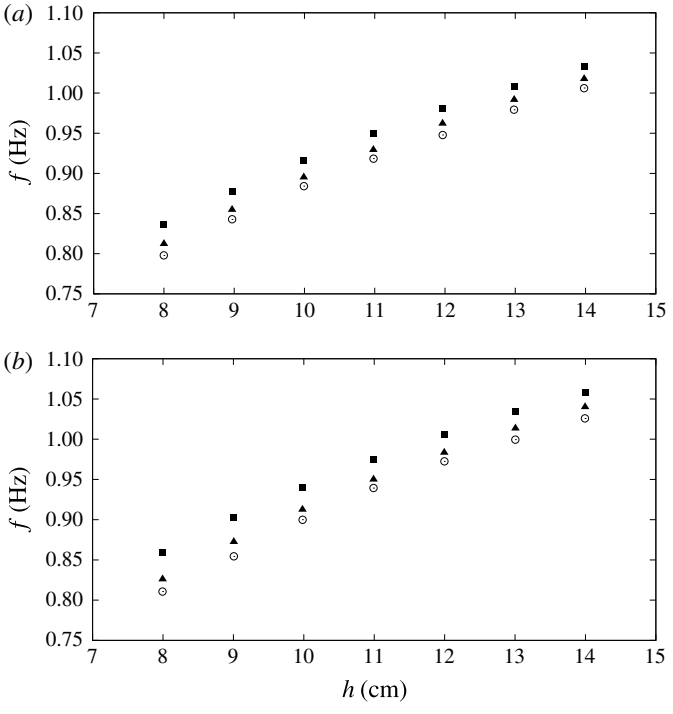

FIGURE 4. Depth variation of the Bragg resonant normal mode frequencies: experimental measurements f_e (open circles) and theoretical predictions f_t (solid triangles) are shown for (*a*) configuration 1 and (*b*) configuration 2. The flat-bottom normal mode frequencies f_9 (solid squares) computed using (4.1) are shown for comparison.

the difference between f_9 and f_t decreases from 2.89 % at $h = 8$ cm to 1.52 % at $h = 14$ cm, whilst for configuration 2 the difference decreases from 3.84 % at $h = 8$ cm to 1.74 % at $h = 14$ cm. Since the effect of bottom corrugations abates as the water depth increases, it is anticipated that the difference between f_t and f_9 will continue to decrease with increasing liquid depth.

4.2. *Time traces*

In each configuration the probes were located to maximize the difference between the oscillation amplitudes but also to avoid placing the probes close to the endwalls. The probes were located at the experimentally determined antinodes and the data were typically collected over 20–30 s intervals. Probes 1 and 2 were always placed on the left and right sides of the tank, respectively. We henceforth denote $a_1(t)$ as the larger-amplitude time series measured at one probe position and $a_2(t)$ as the smaller-amplitude time series measured at another probe location. It is important to understand that these amplitudes are measured by different probes in the two configurations. In configuration 1, the larger-amplitude time series is recorded by probe 1 and the smaller-amplitude time series is recorded by probe 2; in configuration 2, the opposite is true.

Time-series data, simultaneously recorded for both probes using pressure sensors, were obtained at $h = 8,\ 10,\ 12,\ 14$ cm. Comparison with theoretical results are given

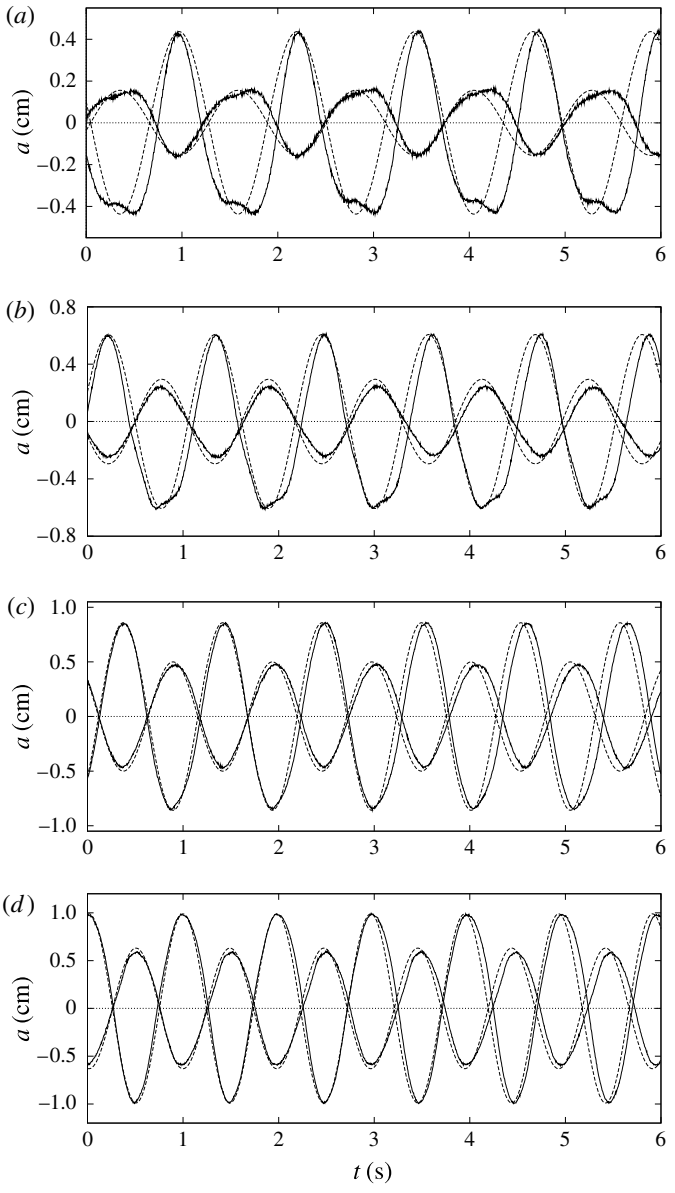

FIGURE 5. Sample large-amplitude $a_1(t)$ and small-amplitude $a_2(t)$ time series from Data Set 1 for configuration 1: (*a*) $h = 8$ cm, $f_e = 0.798$ Hz, $f_t = 0.812$ Hz; (*b*) $h = 10$ cm, $f_e = 0.884$ Hz, $f_t = 0.895$ Hz; (*c*) $h = 12$ cm, $f_e = 0.948$ Hz, $f_t = 0.962$ Hz; (*d*) $h = 14$ cm, $f_e = 1.006$ Hz, $f_t = 1.018$ Hz. Solid lines, experimental measurements; dashed lines, theoretical comparisons.

in figure 5 for configuration 1 and in figure 6 for configuration 2. The solid lines in figure 5 for configuration 1 show the out-of-phase time series for probes separated by $2.5\overline{\lambda}_e$, while those in figure 6 for configuration 2 show in-phase time series for probes separated by $2\overline{\lambda}_e$. Here $\overline{\lambda}_e$ is the mean surface wavelength as defined in the following section. The theoretical sinusoidal time series (dashed lines) are compared to the experimental time series in the following manner.

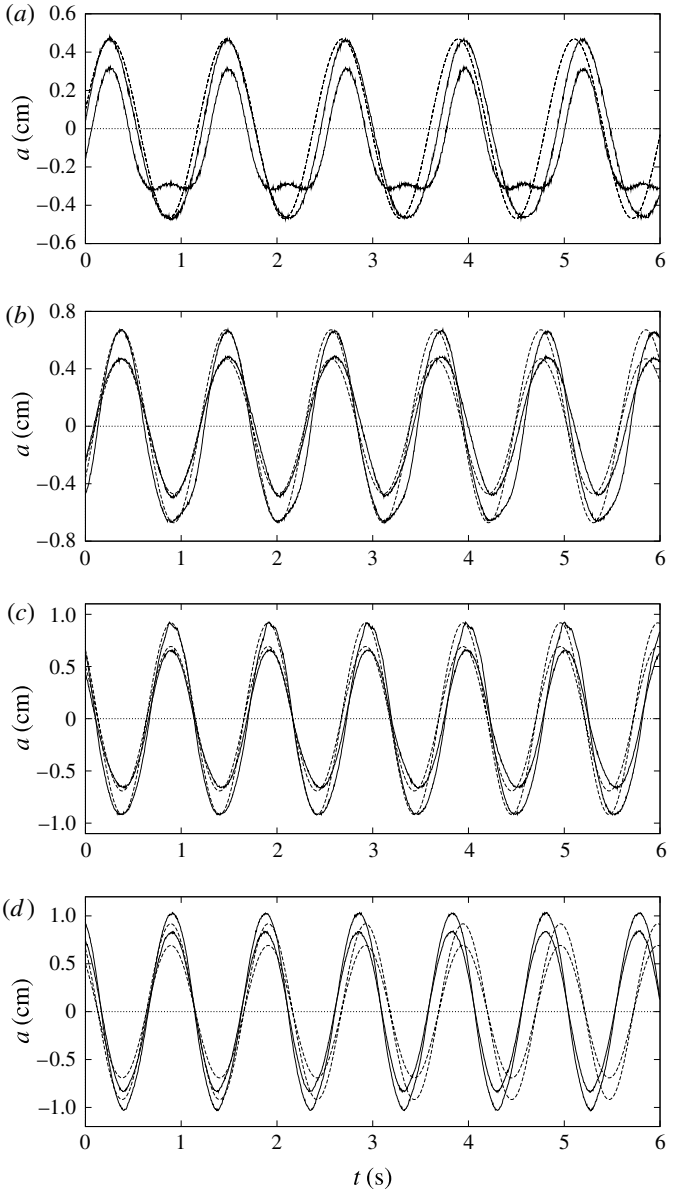

FIGURE 6. Sample large-amplitude $a_1(t)$ and small-amplitude $a_2(t)$ time series from Data Set 1 for configuration 2: (*a*) $h = 8$ cm, $f_e = 0.811$ Hz, $f_t = 0.826$ Hz; (*b*) $h = 10$ cm, $f_e = 0.900$ Hz, $f_t = 0.913$ Hz; (*c*) $h = 12$ cm, $f_e = 0.973$ Hz, $f_t = 0.983$ Hz; (*d*) $h = 14$ cm, $f_e = 1.026$ Hz, $f_t = 1.004$ Hz. Solid lines, experimental measurements; dashed lines, theoretical comparisons.

The amplitude of the free-surface waves for the given horizontal displacement of the tank cannot be determined from the linear theory outlined in § 2. Thus, the theoretical amplitude was set equal to the larger experimental amplitude $a_1(t)$ and aligned in phase at $t \simeq 0$. Then the smaller theoretical amplitude was calculated from the theoretical amplitude ratio (cf. figure 8 introduced in the next section) and these

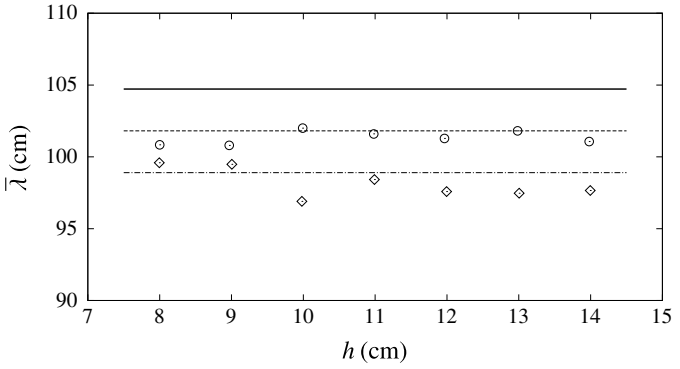

FIGURE 7. Mean free-surface wavelengths as a function of water depth. For configuration 1: experimental measurements $\overline{\lambda}_e$ (open circles) and theoretical estimate $\overline{\lambda}_t$ (dashed line). For configuration 2: experimental measurements $\overline{\lambda}_e$ (open diamonds) and theoretical estimate $\overline{\lambda}_t$ (dash-dot-dash line). The solid line is $2\lambda_{bar}$.

time series were then evolved forwards in time at the theoretical frequency f_t. In both configurations, figure 4 shows that f_t is slightly greater than f_e.

4.3. *Mean wavelengths and amplitude ratios*

The resonant surface waves are not sinusoidal in x over the corrugated-bottom topography, in contrast to the flat-bottom case. For Bragg resonant waves, they are not even spatially periodic because of the slow exponential modulation in the wave amplitude. Strictly speaking, these waves have no wavelengths. For Bragg resonant normal modes, i.e. those with frequencies falling into the resonance tongues, the eigenfunctions will look locally much like standing waves (apart from the immediate neighbourhood of the endwalls), but with amplitudes varying along the tank. The 'wavelengths' of such standing waves may be defined as some kind of average distance between surface nodes.

In the experiments, the mean surface wavelengths $\overline{\lambda}_e$ were measured directly for each configuration at the various water depths. This was accomplished by measuring the horizontal distance between well-defined widely separated nodes and backing out the average wavelength over that distance. The depth variation of the measured mean wavelengths $\overline{\lambda}_e$ are plotted in figure 7. It should be pointed out that the node near the right endwall for configuration 2 is never stationary – it moved to and fro about 1–1.5 cm depending on water depth.

The theoretical prediction of mean wavelength can be accurately determined from the waveforms computed, but a simpler approach can be taken, as follows. For a flat-bottom tank, the wavelength of the mth normal mode is $2L/m$, where L is the total tank length. Although this is not quite appropriate for our tank with a corrugated bottom, it nevertheless can be adopted to obtain a simple, yet adequate, estimate of the mean wavelength, considering that the frequency of the normal mode is not significantly perturbed by the corrugations (cf. figure 4), and that the spatial modulation is slow. For our tank, it is the ninth mode that is Bragg resonant. Thus, for configuration 1, $L = 458.2$ cm gives a theoretical estimate of the mean wavelength $\overline{\lambda}_t = 2 \times 458.2/9 = 101.8$ cm, whilst for configuration 2, $L = 445.1$ cm gives $\overline{\lambda}_t = 98.9$ cm. These mean wavelength estimates are compared with the experimental data in figure 7.

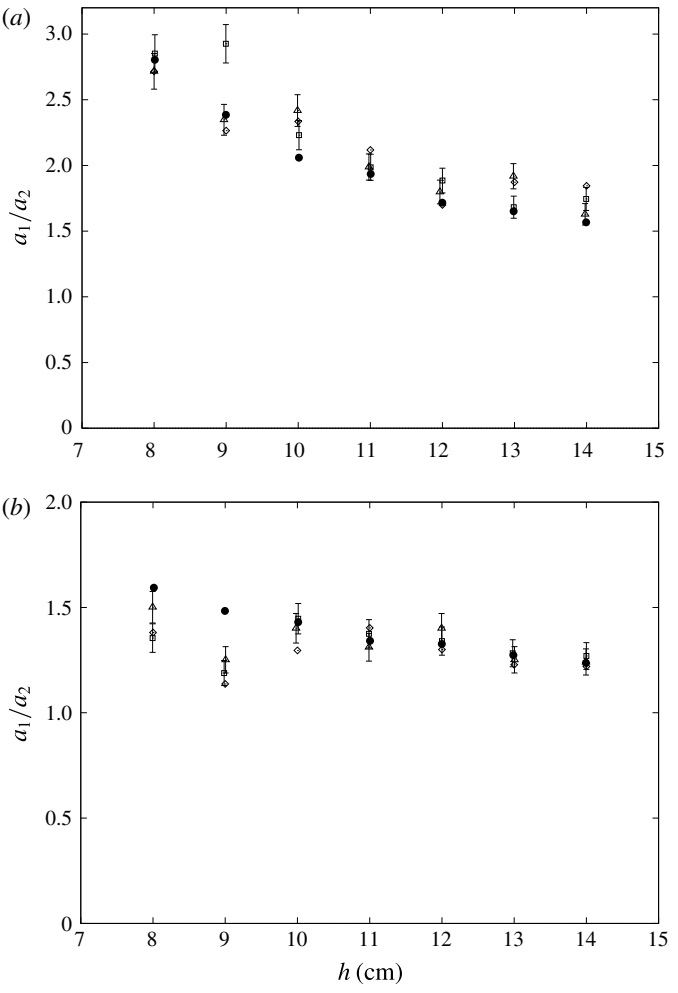

FIGURE 8. Amplitude ratios as a function of water depth: Data Sets 1 (open triangles), 2 (open squares) and 3 (open diamonds) and theoretical predictions (solid circles) for (*a*) configuration 1 with probe separation distance $2.5\overline{\lambda}_e$ and (*b*) configuration 2 with effective probe separation distance $1.5\overline{\lambda}_e$ The error bars on the pressure sensor data come from the analysis in appendix A.

The experimental amplitude ratios were determined as the ratio of the peak-to-peak values of $a_1(t)$ recorded at one tank location to the peak-to-peak values of $a_2(t)$ recorded at another well-separated location. Note that in figures 5(*a*) and 6(*a*), where the signals are not sinusoidal, the peak-to-peak amplitude is taken as the true maximum minus the true minimum of the time series. The amplitude ratios for both configurations obtained from Data Sets 1, 2 and 3 are compared with theoretical estimates in figure 8. The error bars on the pressure probe data from Data Sets 1 and 2 are taken from the analysis in appendix A. The rather large amplitude ratio obtained from Data Set 2 at $h = 9$ cm in configuration 1 provided the motivation to repeat the experiment using the capacitance probe. It is seen that the $h = 9$ cm data point from capacitance probe Data Set 3 is indeed in good agreement with the corresponding measurement from Data Set 1 and with theory. A possible explanation

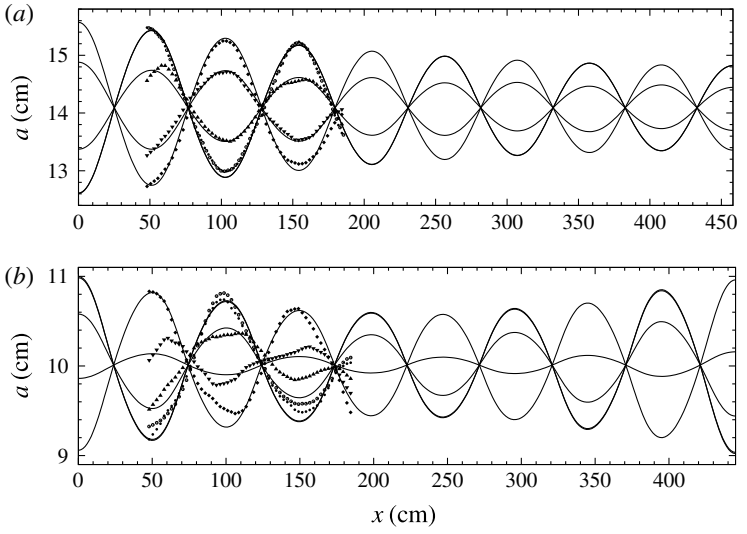

FIGURE 9. Surface waveforms for Bragg resonant normal modes. (*a*) Configuration 1 at depth $h = 14$ cm for which $f_e = 1.0076$ Hz and $f_t = 1.0182$ Hz. Experimental data given at: $t = 0$ s (circles), 0.1666 s (up triangles), 0.333 s (down triangles), 0.50 s (diamonds) and 0.963 s (open circles). (*b*) Configuration 2 at depth $h = 10$ cm for which $f_e = 0.9042$ Hz and $f_t = 0.9133$ Hz. Experimental data given at: $t = 0$ s (circles), 0.1666 s (up triangles), 0.30 s (down triangles), 0.50 s (diamonds) and 0.996 s (open circles). The corresponding theoretical waveforms are plotted as solid lines.

for the outlier in Data Set 2 is that a small water drop was still lodged in one of the brass tubes. It is reassuring in figure 8 to find that the measurements obtained using the capacitance probe (diamonds) are in fundamental agreement with the measurements obtained using the PASCO pressure sensors (triangles and squares).

When assessing the variation of the amplitude ratios with depth presented in figure 8, we realized, *post factum*, that our placement of the left probe for configuration 2 was not optimum – in all cases the left probe was placed at the first antinode to the left of the centre of the tank. Since the centre of the tank for configuration 2 is a node, this means that the left probe was placed $(1/4)\overline{\lambda}_e$ to the left of centre. Thus the wave amplitude decreased from the left probe to the tank centre and then increased towards the right probe placed $2\overline{\lambda}_e$ away. By symmetry we may assume that the left probe measured the same amplitude as if it were placed $(1/4)\overline{\lambda}_e$ to the right of centre, where the waveform is increasing towards the right endwall. Thus the effective separation between the probes from the point of view of amplitude growth is only $1.5\overline{\lambda}_e$. This goes a long way to explain why the variation of the amplitude ratio a_1/a_2 is much smaller for configuration 2 compared to that for configuration 1.

4.4. *Free-surface waveforms*

Waveforms $a(x)$ near the left endwall obtained from video frames are compared with theoretical predictions in figure 9. The experimental data were searched to find the largest waveform amplitude and this was identified as the $t = 0$ data set. The theoretical surface elevations were obtained as follows. The theoretical waveform was

first aligned to be in phase with the experimental data. Then the theoretical amplitude was scaled to best match the two middle maxima in the experimental data. Having set the phase and amplitude at $t = 0$, the theoretical waveforms are calculated at successive experimental times without any further adjustment.

The experimental data at five different times are compared to the theoretical waveforms for $h = 14$ cm in figure 9(*a*) for configuration 1 and for $h = 10$ cm in figure 9(*b*) for configuration 2.

4.5. *Frequency response curves*

To elucidate the behaviour of the system near resonance, measurements of the oscillation amplitude a as a function of frequency f were taken in both configurations at depths $h = 10,\ 12$ and 14 cm. In all six cases, one of the pressure probes was fixed at an experimentally determined position of a local maximum of surface oscillation. Amplitude data were then recorded while gradually sweeping frequencies through the resonance frequency from below.

The experimental results are plotted in figure 10. Each data set was fitted by trial and error with a single-peak Lorentzian function, suggested by the standard theory of resonance for a forced, damped, harmonic oscillator. The particular form of the Lorentzian employed for these fits corresponds to the case when the forcing is imparted by periodic displacement of the support to which the oscillator is attached, in accordance with the experimental procedure described in § 3.1, *viz.*

$$a(f) = \frac{a_0 f^2}{\sqrt{(f^2 - f_{res}^2)^2 + \gamma^2 f^2}}. \tag{4.2}$$

While γ is a measure of the damping relative to the inertia of the system for an actual mass–spring–dashpot simple harmonic oscillator, here it is effectively just a fitting parameter in (4.2). In fact the maximum response in (4.2) does not occur exactly at f_{res}, but it is very nearly so when $\gamma/f_{res} \ll 1$, which is found to hold in all cases of interest here. For the amplitude curve in (4.2), the full width at half-maximum (FWHM) is $\sqrt{3}\gamma$. Clearly the fits thus obtained are heuristic, as a tank partially filled with water is very different from a simple mass–spring oscillator. Nevertheless, the response curves do give a clear indication that the frequencies of the Bragg resonant normal modes can be accurately determined experimentally by adjusting parameters a_0 and γ, and that they exhibit the usual Lorentzian shape. Fits of this kind could be made near any of the resonances of the system, but it is only those in which Bragg reflection plays an important role that are of interest in this paper.

5. Summary, discussion and conclusion

An experimental investigation has been carried out to study Bragg resonant standing waves (normal modes) in a long rectangular water tank with a sinusoidal bottom corrugation. One of the main objectives was to test some theoretical predictions of Howard & Yu (2007), in particular that normal modes with frequencies close to the Bragg resonance frequency have amplitudes modulated over the length of the tank, with the details of this modulation depending sensitively on the phase of bottom corrugations at each endwall. Two cases were tested: configuration 1 corresponding to monotonic exponential growth from the right endwall to the left; and configuration 2 corresponding to amplitudes increasing from the centre towards each endwall.

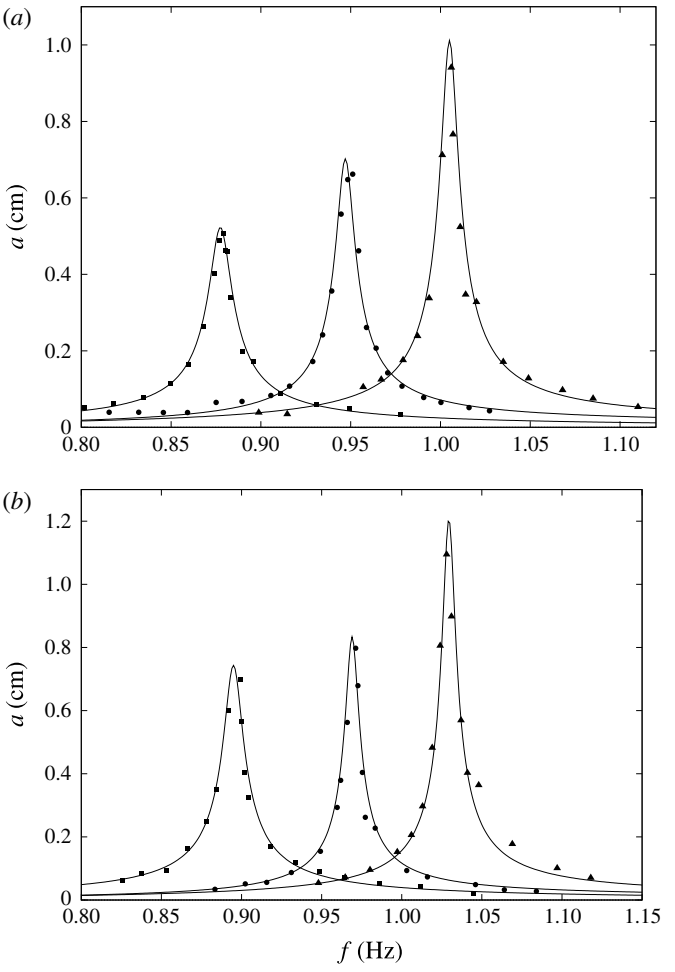

FIGURE 10. Frequency response curves at $h = 10$ cm (squares), $h = 12$ cm (circles) and $h = 14$ cm (triangles) for (a) configuration 1 and (b) configuration 2.

The only difference between the two configurations is a quarter bottom corrugation wavelength shift of the right endwall. Experimental data for each configuration were gathered at seven mean water depths ranging from 8 to 14 cm. We now assess the quality of agreement between measurements and theoretical predictions and comment on the results.

5.1. *Time traces*

In both cases, the time series become less sinusoidal as the water depth decreases, losing the crest–trough symmetry, even with the appearance of secondary peaks at the troughs of the signals (cf. figures 5(a) and 6(a) for $h = 8$ cm). We do not know precisely what has caused the secondary crests at low depth. These features may have similarity to nonlinear Stokes waves, a problem studied in some detail by Kirby (1986*b*), but that is not at all clear. Quadratic nonlinearity can give rise to standing

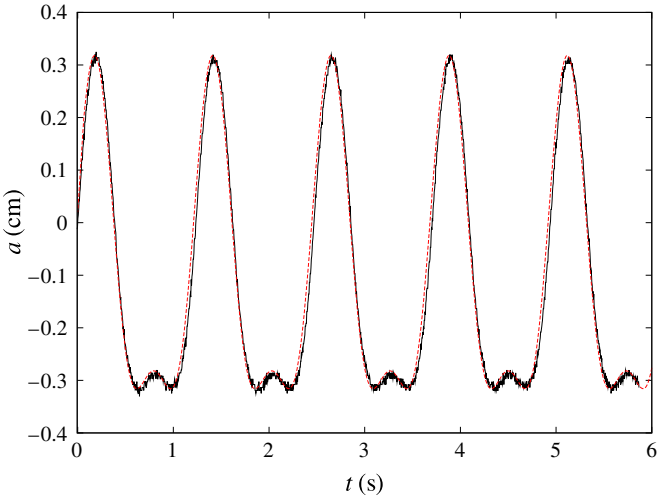

FIGURE 11. (Colour online) Comparison of the small-amplitude time series $a_2(t)$ (solid line) in figure 6(*b*) for configuration 2 at $h = 8$ cm with the fitted time series (dashed line) given in (5.1) for $a_0 = 3$ cm, $\delta = 0$, $b_0 = 0.12$ and $\omega = 5.0876$ rad s^{-1} as obtained from an FFT of the measured time series. The fitted curve can be viewed as the dashed line (red online).

surface wave structure of the form

$$a(t) = a_0 \cos(\omega t) + b_0 \cos(2\omega t + \delta). \tag{5.1}$$

The largest deviation from sinusoidal behaviour occurs for the smaller-amplitude trace $a_2(t)$ in figure 6(*a*) corresponding to configuration 2. To produce a fitted curve of the form (5.1), we took a fast Fourier transform (FFT) of this time series and found that virtually all of the energy is contained in two dominant frequencies, $\omega_1 = 5.0876$ rad s^{-1} (0.80972 Hz) and $\omega_2 = 2\omega_1$. As expected, the fundamental frequency is very close to the measured resonant frequency $f_e = 0.811$ Hz. After aligning (5.1) with the first maximum of $a_2(t)$, we find that $a_0 = 0.3$ cm, $\delta = 0$, $b_0 = 0.12$ cm give a remarkably good fit to the measured time series using the FFT frequency 5.0876 rad s^{-1}, as shown in figure 11. Thus, one might conclude that lowering the water depth brings quadratic nonlinearity to the system. However, for both configurations the standard measure a/h of nonlinearity is quite small, decreasing monotonically from $a/h \sim 0.08$ at $h = 14$ cm to $a/h \sim 0.06$ at $h = 8$ cm. Note that, as a/h decreases, the relative importance of dissipation in the system increases, in qualitative agreement with the variation of the fitting parameter γ observed in figure 10; see § 4.5.

The effect of bottom corrugation amplitude a_{bar} at low depths must also be considered. The ratio $h/a_{bar} = 5.59$ at $h = 14$ cm monotonically decreases to $h/a_{bar} = 3.20$ at $h = 8$ cm. Note that in the region $-1 < h/a_{bar} < 1$ the fluid is completely contained in eight separate 'sinusoidal' basins in which Bragg resonance cannot occur – sloshing in the individual basins is the only possible motion. Therefore, Bragg resonance can only exist for liquid depths $h/a_{bar} > 1$. Indeed, for values of h/a_{bar} only slightly greater than unity, the motion is likely to be dominated by whatever motion (quiescent or sloshing) exists in the separate basins. Thus the appearance of the lobes in figure 11 is likely to depend sensitively on h/a_{bar}.

Nonlinear analyses of horizontally extended wave motion over sinusoidal bottom topography have been reported by Kirby (1986*b*), Sammarco, Mei & Trulsen (1994) and Liu & Yue (1998), and very recently by Xu, Zhiliang & Liao (2015), among others. Unfortunately, only the paper by Sammarco *et al.* (1994) provides actual waveforms, while the other studies only report reflection coefficients; moreover, none of these studies relate to the current investigation of Bragg resonance in a bounded tank. Consequently, the role of nonlinearity in our system must be viewed as a subject for future study. All we can say at present is that the degeneration of linear sinusoidal Bragg waves, at the fixed forcing in our experiment, depends on both h/a_{bar} (waves directly interacting with the bottom corrugations) and a/h (nonlinear effects).

5.2. *Frequencies*

Good agreement is observed between the measured resonant frequencies f_e and the theoretical frequencies f_t at all water depths, though the experimental values always lie slightly below the theoretical predictions; the correspondence comes into better agreement as the liquid depth increases. As is anticipated (cf. § 2.2), the frequency of the normal mode is slightly altered by the presence of bottom corrugations, and here again f_t comes into closer agreement with f_9 as the liquid depth increases.

5.3. *Wavelengths*

The mean wavelength comparison is very good. Slightly greater deviation of $\overline{\lambda}_e$ from $\overline{\lambda}_t$ is observed for configuration 2. This is attributed to the difficulty in determining the position of the fluctuating node near the right endwall used for making measurements of $\overline{\lambda}_e$. For both configurations, the mean wavelengths of the resonant normal modes are bounded from above by $2\lambda_{bar}$, which is the wavelength of a flat-bottom wave having Bragg frequency ω_B (i.e. the resonant wavelength predicted as the amplitude parameter $\epsilon \to 0$). For finite ϵ, we have arranged things so that both configurations have a normal mode with frequency in the 'resonance tongue' (cf. § 2.2); but it is a matter of detailed computation to see which configuration has the higher frequency (or mean wavelength) and how they are related to the flat-bottom Bragg frequency ω_B. For the experimental conditions reported here and plotted in figure 7, $\overline{\lambda}_e$ for configuration 2 lie below $\overline{\lambda}_e$ for configuration 1 which are themselves below $2\lambda_{bar}$. However, it cannot be expected that this arrangement will always prevail.

5.4. *Amplitude ratios*

Unlike the smooth variations of measured frequencies with fluid depth, figure 8 exhibits considerable scatter in the measured amplitude ratios relative to the theoretical predictions in both configurations, even taking into account error estimates for measurements made using the pressure sensors. It should be noted that the error analysis for amplitude ratio measurement in appendix A only pertains to operation of the pressure sensor and does not include other sources of error such as the slightly drifting frequency during the time of measurement, the slight bowing of the tank walls, and the slight bending of the bottom surface of the tank due to the three-point suspension system. It is also noted that the differences between data taken from the first and second series of measurements using pressure sensors, and those taken using the capacitance probe, give a measure of the overall amplitude ratio error in the system.

Despite the scatter, there is qualitative agreement between the theory and experiment – the ratio of oscillation amplitudes decreases as the water depth increases, as expected. At larger depths, the surface wave motion is less affected by the bottom that is further away. Thus, the effects of Bragg resonance should be reduced as the water depth increases, with the surface oscillations becoming increasingly similar to ordinary standing waves. This is consistent with the measurements in figure 8, which shows the amplitude ratio tending to unity (without spatial modulation) as h increases. It is worth pointing out that, even at the relatively large depth $h = 14$ cm ($k_B h = 0.8394$), the amplitude ratio increases as h decreases by a factor $\sim$1.5 over a distance of 2.5 mean wavelengths for configuration 1, and by a factor $\sim$1.25 over an effective distance of 1.5 mean wavelengths for configuration 2, as a result of Bragg resonance. At the shallow depth $h = 8$ cm ($k_B h = 0.4796$), the amplitude ratio can be as large as 2.8 for configuration 1 and 1.5 for configuration 2.

The rather weak variation of amplitude ratios with fluid depth for configuration 2 compared to that for configuration 1 is clearly due to the fact that the probe separation in the former case ($\sim 1.5\overline{\lambda}_e$) is much shorter than that ($\sim 2.5\overline{\lambda}_e$) in the latter case. Assuming for the sake of argument that, over these relatively short distances, the growth rates are linear and equal for the two configurations, then the data for configuration 2 would be increased by a factor of 5/3 to realize the same $2.5\overline{\lambda}_e$ separation as for configuration 1. This would place all the theoretical values in figure 8(*b*) within 24 % of those in figure 8(*a*). While the spatial growth rates are indeed weakly exponential, this simple argument helps to understand the large difference between the amplitude ratio variations with depth in the two configurations.

There are some clear differences in figure 8 between experiment and theory. For configuration 1, the good agreement between theory and measurement at low depths deteriorates as h increases. For configuration 2, the opposite is true: the good agreement between theory and measurement at high depths deteriorates as h decreases. The discrepancy between theory and experiment in the latter case is due, to a great extent, to our definition of the peak-to-peak amplitude that includes the secondary crests at the troughs apparent in figure 6(*a*). However, we have no explanation for the $\sim$10–15 % overshoot in measurement relative to theory for the configuration 1 data at large depths.

Finally, we comment on two sets of measurements visibly different from theoretical prediction. The average of the three experimental points for $h = 10$ cm in figure 8(*a*) lie 13 % above theory while the average of the three experimental points for $h = 9$ cm in figure 8(*b*) lie 20 % below theory. The close grouping of the experimental data suggests that this is a real effect not accounted for by linear theory. In the final analysis, one must bear in mind that the theoretical corrugation profile is only an approximation to the true sinusoidal profile used in the experiment (cf. figure 1) and these differences may have significant effects at low water depths.

5.5. *Spatial waveforms*

General agreement in the spatial variation of the waves over (slightly more than) one wavelength is observed. In figure 9(*a*) for configuration 1 at $h = 14$ cm it is clear that the nodal points are stationary. At this depth, theoretical and measured waveforms are in good agreement except on the left side closest to the left endwall. In figure 9(*b*) for configuration 2 at $h = 10$ cm, the node on the right is again stationary, but the nodal point on the left sways to and fro. This is consistent with the observed vascillation of the nodal point near the right endwall for configuration 2, as pointed out in § 4.3. Here

the measured waveforms compare less favourably to the theoretical calculations. This is due, in part, to the smaller depth where wave distortion starts to become apparent in the time traces shown in figure 6.

In assessing the quality of the comparisons, one must bear in mind a fundamental difference between the theory and experiment: the former is for an inviscid fluid while the latter is viscous. Another fundamental difference is that the theory applies to a stationary tank while in the experiment the tank undergoes small sinusoidal oscillations. If one considers a coordinate system attached to the moving tank, then it can be considered inertial with an extra horizontal body force/unit mass $X_0\omega^2\sin\omega t$, where X_0 is the amplitude of the tank oscillation. However, since observations reveal that the nodal lines near the two endwalls are not stationary, the system deviates from expected inertial behaviour. Thus both viscous effects and the horizontal body force/unit mass need to be considered when comparing experimental and theoretical waveforms near endwalls.

5.6. *Frequency response curves*

The normal mode resonant frequency curves for the two configurations displayed in figure 10 are qualitatively similar – in both cases the peaks decrease as the depths increase. This could be due to the effect of bottom friction, which is expected to become more significant at shallower depths. However, the rate of growth of the peaks with increasing fluid depth is different. Defining $A(h) = a_{max}(h)$ we find for configuration 1 that $A(12)/A(10) = 1.32$ and $A(14)/A(10) = 2.20$. On the other hand, for configuration 2 we find $A(12)/A(10) = 1.14$ and $A(14)/A(10) = 1.97$. Thus the normalized amplitude of the resonance peaks increases more rapidly with depth for configuration 1 compared to configuration 2.

It is clear in both configurations that, while the peak resonance amplitudes increase with liquid depth, the FWHM always decreases with depth. This is consistent with a decreasing dissipation rate (dissipation per unit mass). The decreasing experimental values of FWHM at higher water fills imply, by our heuristic analogy, that the overall dissipation due to the free-surface motions should decrease with h. This trend may be qualitatively explained by noting that the ratio of the dissipation in viscous boundary layers (proportional to the wetted surface area) to the inertia in the system (proportional to liquid volume) decreases with increasing liquid depth. Such an analysis for the present system is well beyond the goals of the present study.

5.7. *Closing remarks*

The experimental approach presented here, developed over the course of extensive study based on three different measuring techniques (resistance wire, new pressure wave gauges and capacitance probes), can now be readily extended to study nonlinear waves and waves over bottom topographies of arbitrary shape. The latter problem is of practical interest for beach erosion prevention, as shore bars are rarely purely sinusoidal (see the review of relevant literature in HY2007). Yu & Howard (2012) proposed recently a linear Floquet theory for any periodic bed, and the present study effectively provides a template for experimental testing of their theoretical results.

We remind the reader that an *a posteriori* benefit of the current work is the development of a new type of wave gauge based on sensing submerged pressures, which, as noted in appendix A, has a distinct advantage over existing pressure wave gauge sensors. The advantage is that it does not depend on knowledge of the wave system, be it linear or nonlinear.

With two notable exceptions in the data for the amplitude ratios, our experimental results agree well with the theory of Howard & Yu (2007) for waves growing exponentially either from one end of the tank to the other (configuration 1), or from the middle of the tank to the endwalls (configuration 2). There are significant differences in waveforms in regions near the endwalls and, more significantly, the linear sinusoidal time series evolves into two-frequency motion as the depth decreases. These new and unanticipated phenomena, absent in the theory, strongly suggest nonlinear effects, and call for further experimental investigation beyond the scope of the present work. It is anticipated that the remaining challenges and open questions, particularly in regard to the role of nonlinearities, will motivate future studies of Bragg resonance in fluid systems.

Acknowledgements

Support of J.Y. by the US National Science Foundation (grants CBET-0756271 and CBET-0845957) during the period of this work is gratefully acknowledged. D. Chebolt, visiting on an internship during the summer of 2008, helped to construct the experimental apparatus, cut the foam corrugations and adapt the motor drive system. Professor C. Felippa computed the points of support for a uniformly loaded channel. The assistance of machinists G. Potts in Mechanical Engineering and M. Rhode in Aerospace Engineering is appreciated. K. Helfrich (WHOI) lent us the wire conductance probes used in the initial study and D. Henderson (Penn State) lent us the capacitance probes and associated electronics. S. Sewell configured our Labview data acquisition system. We are especially grateful to J. Hao of the Computer Science Department at Boston College, who wrote a MATLAB program extracting, in digital form, interface waveforms from our video stills.

In Memoriam. Sadly, our colleague, friend and collaborator Lou Howard passed away on June 28, 2015. Louis N. Howard joined the MIT faculty of Applied Mathematics in 1955 and retired in 1984. Howard was a pillar in the fluid dynamics community, having made seminal contributions to large scale flows in turbulent convection, Hele-Shaw flows, salt-finger zones and, in particular, hydrodynamic stability. He also played an instrumental role in the founding of the Woods Hole Oceanographic Institute Geophysical Fluid Dynamics summer program from its inception in 1959 and attended the summer school every year until he was diagnosed with congestive heart failure in 2010. Howard was a Guggenheim and Sloan Fellow (1961/1962) and a Fairchild Scholar (1976). In 1997 he received the Fluid Dynamics Prize of the American Physical Society. He is a Fellow of the American Physical Society and Member of the National Academy of Sciences. Lou will be missed by friends and colleagues the world over and we are honoured to have him as co-author of this experimental/theoretical endeavour which represents his last JFM publication.

Appendix A. Pressure probe calibration and error analysis

The fact that the water in the tubes acts against a relatively small trapped air volume is fundamental to understanding the operation of the PASCO sensors. Weidman & Kliakhandler (2014) (hereafter referred to as W&K) studied the unsteady gravitational oscillations of a liquid interface in a capped liquid–air column. We use a similar analysis here to analyse the steady variation of air pressure and liquid level in the tube as a function of its level outside the tube.

Consider a vertical tube of length L capped at the top and immersed in a liquid bath. We follow closely the notation of W&K. The vertical coordinates measured from the

bottom of the immersed tube are Y for the liquid outside and Z for the liquid inside. At equilibrium the air pressure in the tube is P_0, not necessarily equal to the ambient air pressure P_a outside the tube. The tube is immersed into the liquid to depth H for arbitrary P_0.

The pressure P_b at the bottom of the tube is given by

$$P_b = P_a + \rho g Y = P + \rho g Z, \tag{A 1}$$

where ρ is the liquid density. Initially $P = P_0$ and $Y = H$, so solution of (A 1) gives the initial liquid rise in the tube as

$$Z_0 = H + \frac{P_a - P_0}{\rho g}. \tag{A 2}$$

For small displacements from equilibrium, W&K have shown that the compression process is isothermal, not adiabatic. Therefore the pressure P of the air trapped in a constant-area tube calculated using Boyle's law is

$$P = \left(\frac{L - Z_0}{L - Z}\right) P_0. \tag{A 3}$$

Using (A 1)–(A 3) and normalizing lengths with H furnishes the equation

$$y - z = \left(\frac{L/H - z_0}{L/H - z}\right) \frac{P_0}{\rho g H} - \frac{P_a}{\rho g H}, \tag{A 4}$$

where the lower-case coordinates y and z are dimensionless. The control parameters $\alpha = (L - h)/H$ and $\beta = P_0/\rho g H$ used in W&K are adopted, and a new parameter $\sigma = P_a/\rho g H$ is introduced. Then (A 2) takes the non-dimensional form

$$z_0 = 1 + \sigma - \beta. \tag{A 5}$$

Equation (A 4) provides a quadratic equation for $z(y)$,

$$z^2 - (\alpha + \sigma + 1 + y)z + (\alpha + 1)(y + \sigma - \beta) + \beta z_0 = 0, \tag{A 6}$$

and from (A 3) the dimensional pressure differential in the tube is

$$P - P_0 = \left(\frac{z - z_0}{\alpha + 1 - z}\right) P_0. \tag{A 7}$$

As noted in figure 2, the brass tubes are connected by tygon tubing to the PASCO pressure sensors. Trapped air resides in the brass tube, in the tygon tube connection and in the PASCO sensor. Storing the volume of all this available air into the constant-area brass tube defines the effective brass tube lengths L for use in the theory, those being $L_1 \doteq 79.346$ cm for probe 1 and $L_2 \doteq 80.072$ cm for probe 2. Recall in the experiment that the connection to the PASCO sensors was made after immersion of the brass tubes in the water. When the air and water are initially at the same temperature, $P_0 = P_a$. Since the brass tubes were blown dry to remove water droplets, they became undercooled relative to the water upon immersion; this implies that the air temperature in a tube rose over time to equilibrate with the ambient water temperature in the tank.

The gravitational constant at the latitude 40.02° N and altitude 2423 m of the experimental site is $g = 9.794$ m s^{-2}, where the ambient pressure $P = 75\,408$ Pa. We take $\rho = 999.1$ kg m^{-3} for the average water density over the temperature range 14–17 °C of the experiment.

Using the above data, (A 6) and (A 7) are solved for the rise height and pressure differential in the liquid column, respectively. In spite of the fact that (A 7) is quadratic, the pressure and liquid displacement exhibit remarkably constant slopes. The rise heights have average slopes $\Delta Z/\Delta Y = 0.090922$ for probe 1 and $\Delta Z/\Delta Y = 0.091697$ for probe 2. This gives the rather unexpected result that for every 1 cm rise in water outside the tube, the water rises only 0.9 mm inside the tube.

Figure 12 shows the dimensional pressure drop $\Delta P = P - P_0$ as a function of dimensional height $Y - H$ for probe 1 calculated from (A 5). The curve is linear with slope 0.08896 kPa cm^{-1}. The maximum experimental amplitude range (MEAR) in our Bragg experiment is indicated. The corresponding result for probe 2 gives a linear curve with slope 0.08888 kPa cm^{-1}. These theoretical results are used to convert pressure measurements using the PASCO sensor into free-surface displacements Y reported in figures 5, 6, 8 and 10.

The effect of an initial overpressure in the tube is now assessed. After blowing dry with compressed air, the brass tubes were mounted in their holders and connected to the PASCO sensors. This procedure took about 5 min, during which time, in the worst-case scenario, it is assumed that the cooled brass tube reduced the air temperature in it and the connecting tygon tubing to the brass tube temperature by conduction. Subsequently, the brass tubes were immersed 2 cm into the water after which the air in the tube warms up owing to the higher temperature of the ambient water and air relative to the undercooled brass tube.

An experiment was performed using a General model IRT205 infrared thermometer. The ambient air temperature measured with the Zoo-Med thermometer was $T_1 = 297.59$ K, assumed equal to the water temperature in the tank. Five minutes after blowing air through the brass tube, its wall temperature was measured at $T_2 = 294.04$ K. It is then assumed that the trapped air warms to the ambient water and surrounding air temperature while the PASCO pressure sensor settles to a constant reading. Using $P_1T_1 = P_2T_2$ gives an overpressure $P_2 = 1.0121P_1$. With little error, we take $P_1 = P_a = 75\,408$ kPa, in which case the overpressure is taken to be $P_0 = P_2$. The resulting pressure drop calculated for probe 1 using (A 7) is plotted in figure 12 as the dashed line. The straight line has slope 0.088099 kPa cm^{-1}, some 0.968 % lower than that without overpressure plotted as the solid line.

We now assess the error in using the pressure probe to measure amplitude ratios. There are four sources of error in the operation of our system: (i) accuracy in vertical placement to the immersion depth estimated to be ±1 mm, (ii) accuracy in the horizontal placement at an antinode estimated to be ±3 mm, (iii) accuracy due to overpressure analysed above, and (iv) accuracy due to probe resolution.

Defining a general error in measurement of wave amplitude as

$$\delta = \pm\frac{\delta a}{a}, \tag{A 8}$$

an analysis readily gives the first three errors as

$$\delta_h = \pm 0.000167, \quad \delta_v = \pm 0.000178, \quad \delta_o = 0.009678, \tag{A 9a–c}$$

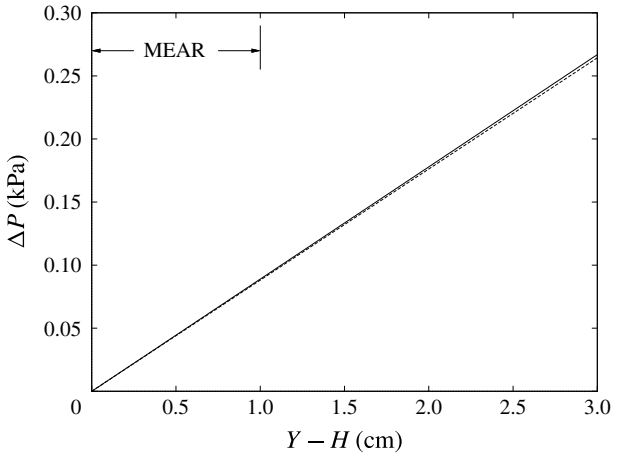

FIGURE 12. Variation of the pressure differential $\Delta P = P - P_0$ with free-surface water level $Y - H$ for probe 1 plotted as the solid line. The maximum effect of an overpressure is plotted as the dashed line. The MEAR for Bragg operation is noted.

in which δ_h is the horizontal placement error, δ_v is the vertical placement error and δ_o is the one-sided overpressure error. Clearly the contributions from placement of the probe are negligible compared to that from the overpressure.

In order to assess the error in the 0.005 kPa resolution of the PASCO probe, we adopt the error in pressure measurement to be half the resolution, just as when you use a ruler with 1 mm markings you can read the length up to ± 0.5 mm. Since the differential pressure is directly proportional to wave amplitude, we take the measurement error due to the probe as $\delta_p = \pm 0.025$. Since the amplitude ratio $R = a_1/a_2$, there are error contributions from measuring both a_1 and a_2 and hence to leading order

$$\frac{\delta R}{R} = \sqrt{(2\delta_p)^2 + (2\delta_o)^2} \doteq 0.052. \tag{A 10}$$

These represent the error bars placed over the amplitude ratio measurements made using the pressure probe in figure 8. Because of the high accuracy of the capacitance probe, no error bars appear on the amplitude ratios measured using that sensor.

We close appendix A by noting that this sensor has distinct advantages over existing pressure wave gauge sensors outlined in the review article by Massel (1996). Massel notes that, although measuring subsurface pressure for evaluation of wave height is practically feasible, an explicit transfer relationship between wave pressure and wave height is needed and some controversy over the adequacy of the transfer function still exists. Wave heights a are related to wave pressure head $H_p = p/\rho g$. The first-order relation between these variables is given by

$$a = \frac{H_p}{K_p}, \quad K_p = \frac{\cosh k(h - z)}{\cosh kh}, \tag{A 11}$$

where K_p is the pressure response factor obtained from linear wave theory in which z is the depth of the pressure sensor under the still water level h and k is the wavenumber. To account for the difference between theory and observation, an

empirical correction factor, N, is usually introduced

$$H = N\frac{H_p}{K_p}, \tag{A 12}$$

and in engineering applications a typical value of $N = 1.25$. However, the value of this correction factor is still in dispute.

Both pressure wave sensors have the same error due to pressure probe resolution. The advantage of pressure wave gauge used in the present study is that it does not depend on knowledge of the waveform it is measuring, be it linear or nonlinear.

REFERENCES

BAGNOLD, R. A. 1946 Motion of waves in shallow water – interaction between waves and sand bottoms. *Proc. R. Soc. Lond.* A **187**, 1–18.

BAILARD, J. A., DEVRIES, J. W. & KIRBY, J. T. 1992 Considerations in using Bragg reflection for storm erosion protection. *J. Waterway Port Coastal Ocean Engng* **118**, 62–74.

BENJAMIN, T. B., BOCZAR-KARAKIEWICZ, B. & PRITCHARD, W. G. 1987 Reflections of water waves in a channel with corrugated bed. *J. Fluid Mech.* **185**, 249–274.

DAVIES, A. G. 1980 Some interactions between surface water waves and ripples and dunes on the seabed. Part 1: the wave-induced flow over seabed topography; Part 2: the reflection of incident wave energy by seabed topography. *Institute of Oceanographic Sciences Report* No. 108, p. 134.

DAVIES, A. G. 1982 The reflection of wave energy by undulations of the seabed. *Dyn. Atmos. Oceans* **6**, 207–232.

DAVIES, A. G. & HEATHERSHAW, A. D. 1983 Surface wave propagation over sinusoidally varying topography: theory and observation. Parts 1 and 2. *Institute of Oceanographic Sciences Report* No. 159, p. 181.

DAVIES, A. G. & HEATHERSHAW, A. D. 1984 Surface wave propagation over sinusoidally varying topography. *J. Fluid Mech.* **144**, 419–443.

DAVIS, A. M. J. & WEIDMAN, P. D. 2000 Asymptotic estimates for two-dimensional sloshing modes. *Phys. Fluids* **12**, 971–978.

HEATHERSHAW, A. D. 1982 Seabed–wave resonance and sand bar growth. *Nature* **296**, 343–345.

HENDERSON, D. M. & HAMMACK, J. L. 1987 Experiments on ripple instabilities. Part 1. Resonant triads. *J. Fluid Mech.* **184**, 15–47.

HOWARD, L. N. & YU, J. 2007 Normal modes of a rectangular tank with corrugated bottom. *J. Fluid Mech.* **593**, 209–234.

KIRBY, J. T. 1986*a* A general wave equation for waves over rippled beds. *J. Fluid Mech.* **162**, 171–186.

KIRBY, J. T. 1986*b* On the gradual reflection of weakly nonlinear Stokes waves in regions of varying topography. *J. Fluid Mech.* **162**, 187–209.

KIRBY, J. T. 1993 A note on Bragg scattering of surface waves by sinusoidal bars. *Phys. Fluids* **5**, 380–386.

KIRBY, J. T. & ANTON, J. P. 1990 Bragg reflection of waves by artificial bars. In *Proceedings of the 22nd International Conference on Coastal Engineering, Delft*, pp. 757–768. ASCE.

LIU, Y. & YUE, D. K. P. 1998 On generalized Bragg scattering of surface waves by bottom ripples. *J. Fluid Mech.* **356**, 297–326.

MASSEL, S. R. 1996 *Ocean Surface Waves: Their Physics and Prediction*, Advanced Series on Ocean Engineering, vol. 11. World Scientific.

MEI, C. C. 1985 Resonant reflection of surface waves by periodic sandbars. *J. Fluid Mech.* **152**, 315–337.

MILNE-THOMSON, L. M. 1962 *Theoretical Hydrodynamics*. Macmillan.

O'HARE, T. J. & DAVIES, A. G. 1993 Sand bar evolution beneath partially-standing waves: laboratory experiments and model simulations. *Cont. Shelf Res.* **13**, 1149–1181.

RILEY, N. 1984 Progressive surface waves on a liquid of non-uniform depth. *Wave Motion* **6**, 15–22.

SAMMARCO, P., MEI, C. C. & TRULSEN, K. 1994 Nonlinear resonance of free surface waves in a current over a sinusoidla bottom: a numerical study. *J. Fluid Mech.* **179**, 377–405.

WEIDMAN, P. D. & KLIAKHANDLER, I. 2014 Gravitational oscillations of a capped liquid–air column. *Phys. Fluids* **26**, 04710,1–21.

XU, D., ZHILIANG, L. & LIAO, S. 2015 Equilibrium states of class-I resonant wave system. *Eur. J. Mech.* (B/*Fluids*) **50**, 38–51.

YU, J. & HOWARD, L. N. 2010 On higher order resonance of water waves by bottom corrugations. *J. Fluid Mech.* **659**, 484–504.

YU, J. & HOWARD, L. N. 2012 Exact Floquet theory for waves over arbitrary periodic topographies. *J. Fluid Mech.* **712**, 451–470.

YU, J. & MEI, C. C. 2000*a* Do longshore bars shelter the shore? *J. Fluid Mech.* **404**, 251–270.

YU, J. & MEI, C. C. 2000*b* Formation of sand bars under surface waves. *J. Fluid Mech.* **416**, 315–348.

YU, J. & ZHENG, G. 2012 Exact solutions for wave propagation over a patch of large bottom corrugations. *J. Fluid Mech.* **713**, 362–375.